NUMERICAL SIMULATION OF SHAPED CHARGE JET PENETRATING A PLATE USING SMOOTHED PARTICLE HYDRODYNAMICS

ZHANG ZHIFAN, MING FUREN AND ZHANG AMAN

College of shipbuilding engineering
Harbin Engineering University, Harbin 150001, China
zhangzhifan@hrbeu.edu.cn, mingfuren2006@126.com, zhangaman@hrbeu.edu.cn

Key words: SPH Method; Shaped Charge Jet; Underwater Explosion; Damage Characteristics.

Abstract. The shaped charge jet has a stronger penetration effect onto the structure than normal charges. The SPH method with mesh-free and Lagrange properties has an advantage to solve extremely dynamic problems, such as large-deformation, moving interface and multiphase mixing and so on. Therefore, the SPH method is applied to simulate shaped charge detonation, jet formation and its penetration into a plate. And a SPH model of the shaped charge penetrating the plate is established. Firstly, the simulation of the shaped charge detonation is conducted to study the shock wave propagation and underwater explosion shock loading. Secondly, the formation of the metal jet is studied, and the jet velocity and the pressure are investigated in detail. Finally, the damage characteristics of the plate subjected to the metal jet and underwater explosion shock loading are discussed. The whole analysis and conclusions provide a reference for the structural design of shaped charge warheads.

1 INTRODUCTION

The shaped charge jet (SCJ) associated with underwater explosion can cause server damages to warships and submarines; it is one of the major threats and research focuses of navy platform technology. The three stages, namely detonation, formation of the metallic jet and its impact on the target plate, are included when a plate is penetrated by the metal jet. Although experimental research [1-5] is the most effective and direct countermeasure to investigate the formation of the jet and the SCJ penetration, it has disadvantages of less-safety and high-cost as well as unrepeatability. Therefore, numerical method is usually combined with experiments to study the performance of shaped charge. Modeling and simulation have been used to develop the shaped charge and test configuration by Baker [6]. Basic investigations were continued with theoretical studies supporting the findings in [7] by numerical simulations of the SCJ perforation [8]. Cheng [9] has employed some real explosion test data regarding the perforation size and penetration depth to verify the numerical simulation.

However, large deformation of liner, steel and explosion products may be caused during the jet penetrating the plate, and there will be computational difficulties (e.g. grid distortion) to be overcome while using the finite element method [10-12] as a result. The Smoothed Particle Hydrodynamics (SPH) method [13-20] has natural advantages in simulating the SCJ penetration and underwater explosion because its mesh-less nature is suitable for solving

problems of large deformation, and its Lagrangian nature makes it extremely easy to capture material interfaces. In addition, explosively-formed projectile (EFP), a new kind of shaped charge, has higher penetration ability. Therefore, the SPH method is adopted to simulate the shaped charge jet (SCJ) associated with underwater explosion, with the analysis of characteristics of shock wave propagation, the formation process of metal jet (EFP formation with hemispherical liner) and damage characteristics of the plate.

2 THEORETICAL BACKGROUND

2.1 SPH Equations of Motion

In SPH method, the approximation of function $f(x)$ and its derivative $\nabla \cdot f(x)$ can be discretized as [21]

$$f(\boldsymbol{x}_i) \approx \sum_j \frac{m_j}{\rho_j} f(\boldsymbol{x}_j) W_{ij} \tag{1}$$

$$\nabla \cdot f(\boldsymbol{x}_i) \approx \sum_{j=1}^{N} \frac{m_j}{\rho_j} f(\boldsymbol{x}_j) \cdot \nabla_i W_{ij} \tag{2}$$

Thus, the conservation of mass, momentum and energy in SPH can be expressed as (regardless of body force) [21, 22]:

$$\begin{bmatrix} \dfrac{d\rho_i}{dt} \\[2mm] \dfrac{d\boldsymbol{v}_i^a}{dt} \\[2mm] \dfrac{de_i}{dt} \end{bmatrix} = \begin{bmatrix} m_i \displaystyle\sum_{j=1}^{N} \boldsymbol{v}_{ij}^b \\[2mm] -\displaystyle\sum_{j=1}^{N} \frac{m_j}{\rho_j}\left(\frac{\sigma_i^{ab}+\sigma_j^{ab}}{\rho_i}+\Pi_{ij}\right) \\[2mm] \dfrac{1}{2}\displaystyle\sum_{j=1}^{N} \frac{m_j}{\rho_j}\left(\frac{\sigma_i^{ab}+\sigma_j^{ab}}{\rho_i}+\Pi_{ij}\right)\boldsymbol{v}_{ij}^b \end{bmatrix} \cdot \frac{\partial W_{ij}}{\partial \boldsymbol{x}_i^b} \tag{3}$$

where ρ, m, v, e, t, x, σ denote density, mass, velocity, energy, time, coordinates and stress respectively; a and b indicate the direction along axis; W_{ij} is the smoothed function of a pair of particles i and j, the cubic spline function is applied in present paper; Π_{ij} represents artificial viscosity [21].

2.2 Constitutive model

In the process of strong impact such as underwater explosion, the viscosity of water and exploding gas is small and can be ignored. The pressure of detonation products and water can be obtained from Jones-Wilkins-Lee (JWL) EOS [23] and Mie-Gruneisen equation of state [24] respectively.
Jones-Wilkins-Lee (JWL) EOS [23] for explosive gas is given by

$$P = A(1 - \frac{\omega\eta}{R_1})e^{-\frac{R_1}{\eta}} + B(1 - \frac{\omega\eta}{R_2})e^{-\frac{R_2}{\eta}} + \omega\eta\rho_0 e \tag{4}$$

where ρ_0 is initial density; D is detonation velocity; A, B, R_1, R_2 and ω are experimental fitting coefficients; E_0 is detonation energy per unit mass. Parameters are shown in Tab. 1.

Table 1 Parameters in Jones-Wilkins-Lee (JWL) EOS for explosive gas [23]

$\rho_0(\mathrm{kg/m^3})$	$D(\mathrm{m/s})$	$A(\mathrm{Pa})$	$B(\mathrm{Pa})$	R_1	R_2	ω	$E_0(\mathrm{J/kg})$
1630	6930	3.74	3.75	4.15	0.90	0.35	6.0×10^6

Mie-Gruneisen equation of state [24] for water is expressed as

$$P = \begin{cases} \dfrac{\rho_0 C^2 \mu[1 + (1 - \frac{\gamma_0}{2})\mu - \frac{a}{2}\mu^2]}{[1 - (S_1 - 1)\mu - S_2 \frac{\mu^2}{\mu+1} - S_3 \frac{\mu^3}{(\mu+1)^2}]^2} + (\gamma_0 + a\mu)e & \mu > 0 \\[4mm] \rho_0 C_0^2 \mu + (\gamma_0 + a\mu)e & \mu < 0 \end{cases} \tag{5}$$

where ρ_0, C, η, a and E_0 denote initial density, sound velocity, density ratio before and after the perturbation, volume correction coefficient and initial energy respectively; S_1, S_2 and S_3 are fitting coefficients. Parameters are shown in Tab. 2.

Table 2 Parameters in Mie-Gruneisen EOS for water [24]

$\rho_0(\mathrm{kg/m^3})$	$C(\mathrm{m/s})$	γ_0	a	S_1	S_2	S_3	$E_0(\mathrm{J/kg})$
998	1480	0.5	0	2.56	1.986	1.2268	357.1

However, the shear force of steel and copper with high shear strength should be taken into account. Steel and copper are used as the materials of the plate and the liner, respectively. The stress is composed of isotropic pressure P and deviatoric stress tensor S. For pressure P, Mie-Gruneisen EOS for solid mechanics [25] is introduced, given by

$$P = \left(1 - \frac{1}{2}\Gamma\eta\right) \cdot \left(\alpha\eta + \beta\eta^2 + \gamma\eta^3\right) + \Gamma\rho e \tag{6}$$

where Γ is Gruneisen parameter; if η is less than 0, $\beta = \gamma = 0$; $\alpha = \rho_0 C_s^2$, $\beta = \alpha[1 + 2(S_s - 1)]$ and $\gamma = \alpha[2(S_s - 1) + 3(S_s - 1)^2]$, in which ρ_0, C_s, S_s and E_0 denote initial density, linear

participation coefficient of impact velocity and particles velocity, slope and initial energy. Parameters are shown in Tab. 3.

Table 3 Parameters in Mie-Gruneisen EOS for steel and copper [25]

Material	$\rho_0(\text{kg/m}^3)$	Γ	$C_s(\text{m/s})$	S_s	$E_0(\text{J/kg})$
steel	7890	1.587	3075	1.294	0
copper	8960	2.0	3940	1.489	0

As for deviatoric stress tensor S, it be drawn from the stress rate $\dot{S}$ by integration, and yet $\dot{S}$ can be gained from Jaumann stress rate [21]. The Johnson-cook [26] model and Von Mises yield criterion are applied to calculate yield strength and determine whether the stress should be renewed through the comparison between Mises Stress σ_{Mises} and yield strength Y. If Mises Stress is less than the yield strength, there is no need to modify the stress component. On the contrary, the deviatoric stress S should be modified [27]. The Johnson-cook [26] model is given as

$$Y = \left[\sigma_0 + B_0\varepsilon_e^n\right]\left[1 + C\boldsymbol{ln}\left(\dot{\varepsilon}_e / \dot{\varepsilon}_0\right)\right]\left[1 - (T^*)^M\right] \tag{7}$$

where σ_0, C and M denote the static yield strength, strain rate strengthening coefficient and thermal softening coefficient; B and n are strain hardening exponents; ε_e is equivalent plastic strain, i.e. $\varepsilon_e = 2\sqrt{3I_2}/3$, in which I_2 is the second invariant of deviator stress tensor; $\dot{\varepsilon}_e$ and $\dot{\varepsilon}_0$ denote equivalent plastic strain rate and reference strain rate, repectively; T^ϕ is dimensionless temperature corresponding to T, i.e. $T^\phi = (T - T_r)/(T_m - T_r)$, in which T_r is room temperature, T_m is melting temperature and $T = T_r + (e - e_0)/(MC_v)$, in which e, e_0 and C_v denote specific internal energy, initial specific internal energy and specific heat. Some parameters are listed in Table 4.

Table 4 Parameters in Johnson-Cook constitutive model for steel and copper [26]

Material	$\sigma(\text{MPa})$	$B(\text{MPa})$	$\dot{\varepsilon}_0(\text{s}^{-1})$	n	C	m	$T_m(\text{K})$	$T_r(\text{K})$	$C_v(\text{J/kgk})$
steel	350	275	1	0.36	0.022	1.0	1811	288	452
copper	90	292	1	0.31	0.025	1.09	1356	288	383

2.3 Some numerical techniques

(a) Variable Smoothing length

The accuracy and robustness of the SPH processor depends on the quality (in particular the number) of the local neighboring particles. In expansive flow of material, the distance

between SPH particles increases. If this distance exceeds twice the smoothing length of the particles, then the two particles will no longer interact. This loss of interaction may be unphysical and is commonly described as "numerical fracture". In an attempt to reduce the problem of numerical fracture, an option to include a variable smoothing length has been included; as particles separate and their density decreases, their smoothing length increases so that interaction with neighboring particles is maintained [28-30].

(b) Artificial viscosity

The Monaghan Artificial Viscosity [21, 28] has been to spread shocks over a few particle diameters (smoothing lengths), stabilize the numerical scheme and prevent particle penetration. This form of artificial viscosity includes a term which is a function of the local velocity field, a linear term, and one which is a function of the local velocity field squared. Each of these terms has a multiplying coefficient that can be adjusted depending on the type of problem being solved.

(c) Treatment of multi-materials

We use a slight penalty force of Lennard-Jones model [21] to solve interface problem, and the molecular force is so slight that it just prevents particles' penetration. When particles on both sides of an interface tend to penetrate, in the case where $r_0 \geq r_{ij}$, there would be a molecular force $F_{ij} = f \cdot [(r_0 / r_{ij})^a - (r_0 / r_{ij})^b] \cdot x_{ij} / r_{ij}^2$ acting on two approaching particles; where r_0 is cutoff radius and it is generally close to the initial spacing of particles and r_{ij} is the distance between particles i and j. The direction of the F_{ij} is along the center line of the particles, preventing the particle from penetrating; f, a and b are set parameters. Consequently, we use the ratio of r_0 to r_{ij} to deal with the interface; this can guarantee good numerical stability without errors caused by the smoothing length.

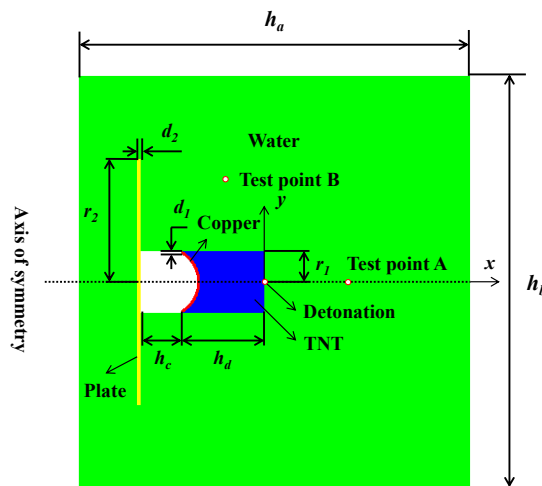# 3 NUMERICAL SIMULATION

3.1 Numerical model

Figure 1 Distribution of particles

The model of shaped charge jet penetrating a plate subjected to underwater explosion can

be simplified as Figure 1. The relevant parameters are listed in Table 5. The material of the liner is copper. The column TNT is detonated from the center which is also the origin of coordinates. Test points A and B are located at (28, 0) and (-16, 43) respectively. The entire model is discretized with non-uniform particle spacing, 0.1m for the plate, copper and TNT and 0.2mm for water. There are 24000 steel particles, 3442 copper particles, 101676 TNT particles and 654500 water particles.

Table 5 Parameters in numerical model (mm)

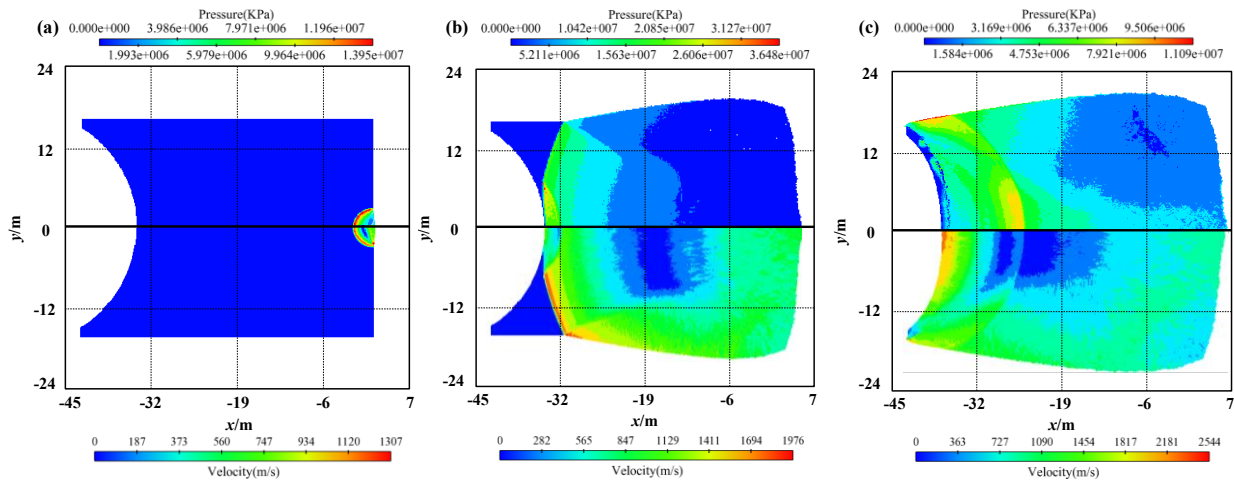| h_a	h_b	h_c	d_1	d_2	r_1	r_2
190	200	20	1.0	2.0	15	60

3.2 Explosion process

Figure 2 Pressure distribution (upper) and velocity distribution (lower) of TNT and copper in the explosion process; from (a) to (c) the times are: $t \approx 0.4\,\mu s$, $4.8\,\mu s$ and $6.4\,\mu s$

Figure 2 illustrates the detonation process of the TNT. It can be seen that a spherical detonation wave is generated after the detonation, with the pressure up to about 14 GPa at 0.4 μs. As Figure 2(a) shows, the velocity on the wavefront reaches about 1307 m/s. After that, the detonation wave propagated with high speed and explosion products continued to expand. At $4.8\,\mu s$, the shock wave reached the liner and the pressure peak value soared to about 36 GPa as shown in Figure 2(b). The velocity rose slightly, peaking at about 1976 m/s on the boundary of explosion products. As can be seen from Figure 2(c), the detonation finishes at around $6.4\,\mu s$ and the maximum pressure declined to about 11 GPa. It can also be observed from the pressure nephogram that there was a rarefaction wave reflected when the shock wave propagated to the liner whose other side is exposed to air. As a result, the pressure of explosion products gradually decreases. Figure 2(c) also shows that the maximum velocity went up to about 2544 m/s and it occurs around the symmetry axis. In addition, it is clear that the liner is accelerated under the tremendous pressure behind it as shown in Figures 2(b) and

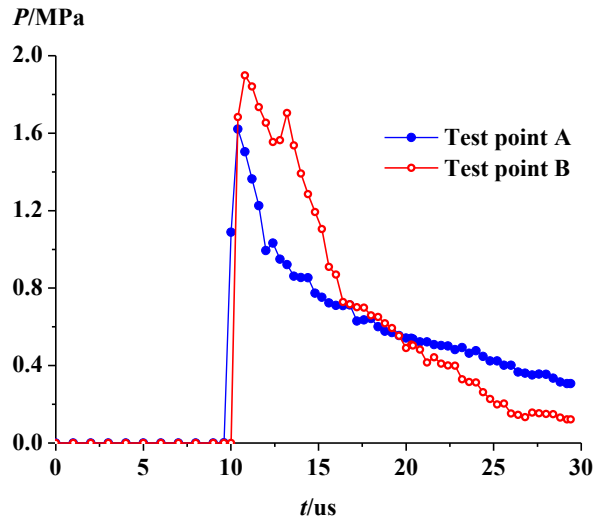2(c). Consequently, the numerical results agree with the basic laws of shock wave propagation.

Figure 3 Pressure-time curve at tests point A and B

The time history curves of the shock wave pressure at test points A and B are shown in Fig. 3. Test points A and B are located in the axial and radial directions in the water area, which are marked in Fig. 2. It can be observed that the shock wave arrives at the test points at around 10 μs, with the pressure shooting up to about 1.6 MPa and 1.9 MPa respectively. Obviously the radial pressure peak value at test point B is higher than that of the axial peak value at test point A. Subsequently, the pressure rapidly declined. There are two peaks of the curves, the first peak is caused by the direct wave of the explosion, and the second peak may just result from the second propagation. As the detonation waves propagating from the TNT to the water, the reflection waves will be generated and subsequently converged at the TNT center, which will lead to the generation of compressive waves back into water again. Comparing these two curves, we can also see that the tangent at point B is larger than that at point A after the pressure reaches the peak value, i.e. the radial pressure drops faster than the axial pressure. It is clear that the radial pressure becomes lower than the axial pressure after 18 μs. Finally, the pressures at test points decrease to about 0.306 MPa and 0.121 MPa at about 30 μs.

3.3 Formation of metal jet

After the detonation of TNT, the metal jet gradually is formed under the effect of the detonation wave. In this section, we will simulate the formation of the metal jet and discuss some variables (e.g. velocity, length and width of the metal jet) at special moments. Fig.4 and Tab. 6 illustrate the velocity distribution of the liner in the formation of metal jet and some variables, respectively.
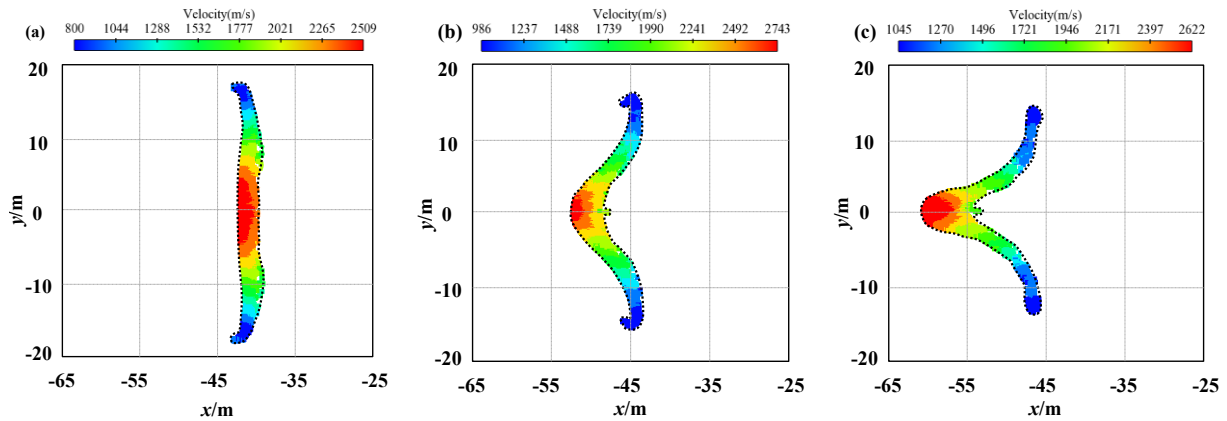
Figure 4 Velocity distribution of copper in the formation of metal jet; from (a) to (c) the times are: $t \approx 9.2\,\mu s$, $12.8\,\mu s$ and $16\,\mu s$

Fig.4 shows the velocity distribution of liner in the formation of metal jet. Hemishperical liner is chosen as the liner. As can be seen from Fig. 4(a), under the effect of the detonation wave of the liner is squeezed and plastic large-deformation of the liner comes out, with the top of the liner rolling over. The detonation products at the end with the hollow cavity converge towards the centerline, i.e. axis of symmetry, at high velocity as high as 2509 m/s. With the deformation of the liner, the pressure turns the original outer surface into inner surface, with the original inner suface converted to the outer surface. Besides, we can see from Fig. 4(b) that due to the effect of axial tension and radial compression, the liner converges to the axis of symmetry, and the initial metal jet (EFP) with a high speed is formed. The velocity reaches its peak at $12.8\,\mu s$ and it is as high as about 2743 m/s. Subsequently, the velocity declines gradually and it dropped to around 2622 m/s at $16\,\mu s$. It can be observed that the inner surface has turned into the jet head and the metal jet is elongated to several times of its initial length as Fig. 4(c) shown.

Table 6 Jet velocity, length and width at special moments (mm)

Parameters of metal jet	Time (μs)		
	9.2	12.8	16.0
Velocity (m/s)	2509	2743	2622
Length (mm)	-	2.2	4.5
Width of jet head (mm)	-	3.6	3.8

Tab. 6 gives the information of parameters of metal jet, namely velocity, length and width, at special moments. At $9.2\,\mu s$, the original inner surface of liner begins to be transformed into the outer surface. The velocity of jet head rises to its maximum at $12.8\,\mu s$. At the same time, the initial metal jet is produced, with the length and width being 2.2 mm and 3.6 mm, respectively. At $16.0\,\mu s$, the metal jet is poised to penetrate the plate. Besides, the length and

the width are larger than the initial ones.
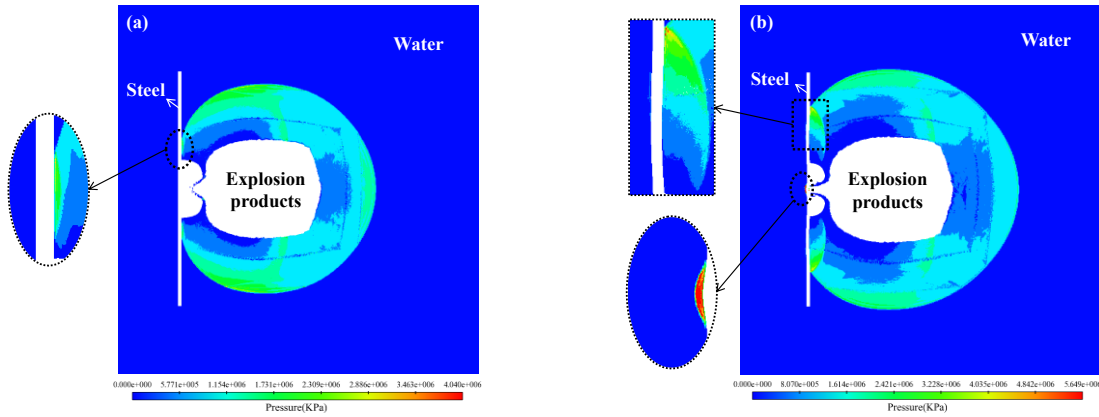
3.4 Metal jet penetrating a plate

Figure 5 Pressure nephogram of water; from (a) to (b) the times are: $t \approx 14.0\,\mu s$ and $16.8\,\mu s$

Pressure nephogram of water is shown as Fig. 5. It is clear that the shock wave reaches the steel at 14.0 μs as shown in Fig. 5(a), and a reflected shock wave is generated in the water as a result, which is presented in the elliptical region. It can also be observed in Fig. 5(a) that the shock wave arrives at the steel earlier than the jet. Subsequently, the reflected shock wave propagates in the water and the directive wave leads to the deformation of the steel, which is shown in the rectangular region in Fig. 5(b). Besides, as the elliptical region in Fig. 5(b) shows, the shock wave generated at the jet head has passed through the steel and arrived at the water on the other side of the steel.
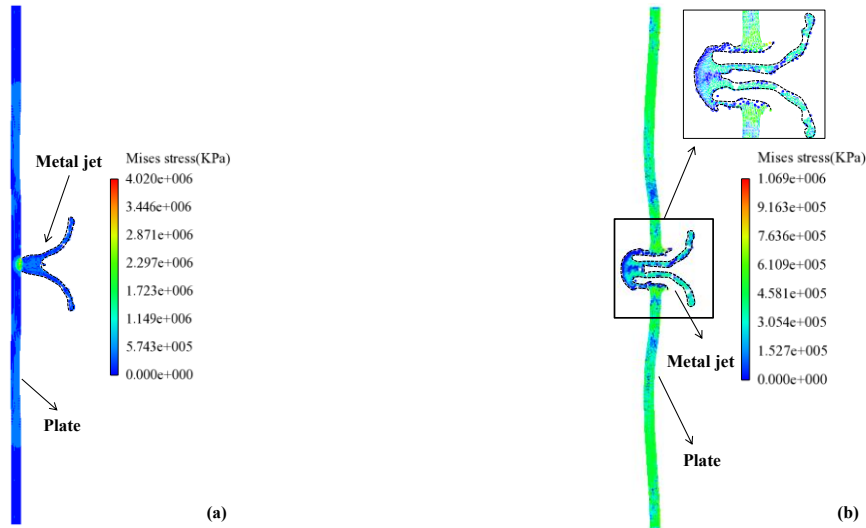

Figure 6 Mises stress distribution of steel and copper; from (a) to (b) the times are: $t \approx 16.4\,\mu s$ and $21.2\,\mu s$

Fig. 6 illustrates mises stress distribution of steel and copper in the process of metal jet penetrating the plate. According to Fig. 6(a), we can see that the jet begins to penetrate the plate, with the stress up to about 4 GPa. Besides, it is clear that there are not only a reflected

shock wave but also a shock wave generated in the steel as shown in Figs. 5(b) and 6(a). After that, the middle of the plate is completely penetrated by the metal jet and the plate subjected to the shock wave load produces deformation at 18.4 µs. At the same time, the stress decreases to about 1.1 GPa at 21.2 µs. In addition, it can be observed that the main failure mode is plastic large-deformation and tensile failure as shown in Fig. 6.
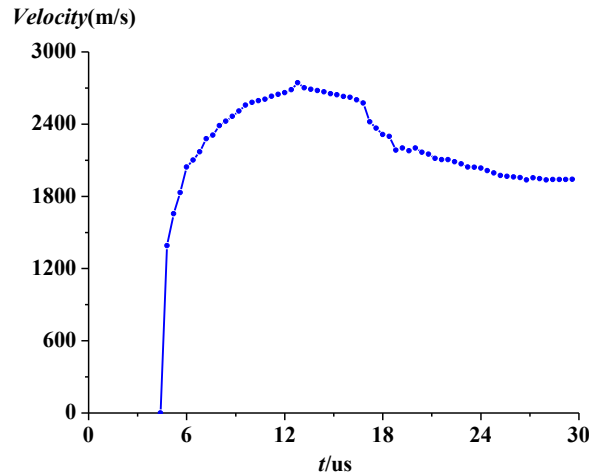

Figure 7 Velocity-time curve of the liner

Velocity-time curve of the liner is shown in Fig. 7. It can be seen that the figure rises dramatically after the detonation wave reaches the liner, peaking at 2743 m/s at 12.8 µs. At this moment, the initial metal jet is formed. After that, the velocity begins to decrease and has slightly dropped to around 2602 m/s at 16.0 µs. Subsequently, due to the impact effect of the jet on the plate, the velocity of the jet falls again but more steeply, reaching about 2297 m/s at 18.4 µs. After the plate is completely penetrated by the metal jet, the velocity experiences a slight decline, with the velocity decreasing to about 2104 m/s at 22 µs. Finally, the curve remained stable at 25.6 µs and the velocity is as high as about 1941 m/s at 29.6 µs.

4 CONCLUSIONS

An SPH method with mesh-free and Lagrange properties is applied to solve extremely dynamic problems of a plate penetrated by shaped charge jet (SCJ) associated with underwater explosion in this paper. The whole process of such a complex physical phenomenon as SCJ penetrating the plate is simulated, including three phases, namely the detonation, the formation of metal jet and the penetration. The following conclusions can be drawn through the analysis of shock wave propagation, jet velocity and damage characteristics of the plate: (a) the numerical results agree with the basic laws of shock wave propagation and the shock wave arrives at the plate prior to the metal jet; (b) the velocity of the jet increases first and then decrease, peaking at about 2743 m/s; (c) the crevasse of the plate is caused by the penetration of the metal jet and the deformation of the plate arises from underwater explosion shock wave as well.

ACKNOWLEDGE

REFERENCES

[1] Kibe, S., Yamamoto, T. and Katayama, M. Development of conical shaped charge and remaining problems. *50th 1AF Congress*, IAA-99-1AA.6.5.03, Amsterdam, 4-8 Oct. (1999).

[2] Hu, G.L., Liu, R.Z. and Li, B. et al. Power Experiments on Compound Torpedo Warhead Assembly. *Journal of Nanjing University of Science and Technology* 29 (2005): 6-8. (in Chinese)

[3] Hornemann, U. and Holzwarth, A. Shaped charge penetration in alumina targets. Int. J. Impact Engng (1997) **20**: 375-386.

[4] Huang, Hongfa. Characterization of Powder Metal Jet and Penetration Calculation. *Procedia Engineering* (2013) **58**: 471-478.

[5] Manfred, H. Disturbance of Shaped Charge Jets by Bulging Armour. *Propellants, Explosives, Pyrotechnics* (2001) **26**: 191–195.

[6] Ernest, L.B., James, P. and Timothy, M. et al. Shaped Charge Jet Characterization and Initiation Test Configuration for IM Threat Testing. *Procedia Engineering* (2013) **58**: 58-67

[7] Werner, A. and Ernst, R. Shaped Charge Jet Initiation Phenomena of Plastic Bonded High Explosives. *Proceedings of the 2012 Insensitive Munitions & Energetic Materials Technology Symposium (IMEMTS)*, Las Vegas, NV, USA, May 14-17. (2012)

[8] Werner, A. and Ernst, R. High Explosive Initiation Behavior by Shaped Charge Jet Impacts. *Procedia Engineering* (2013) **58**: 184-193

[9] Cheng, S.Q., Chen, G.J. and Zhao, H.G. Numerical Damage Analysis of Shaped Charge Warheads on Double-Deck Target Plates. *Chinese Journal of Ship Research* (2013) **8**: 53-57 (in Chinese)

[10] Hans, U.M. Review: hydrocodes for structure response to underwater explosion. *Shock and Vibration* (1999) **6**:81-96.

[11] Benson, D.J. Computational methods in Lagrangian and Eulerian hydrocodes. *Computer Method in Applied Mechanics and Engineering* (1992) **99**: 235-394.

[12] Charles, E. and Anderson, Jr. An overview ofthe theory ofhydrocodes. *International Journal ofImpact Engineering* (1987) **5**: 33-59.

[13] Liu, M.B., Liu, G.R. and Lam, K.Y. Comparative study of the real and artificial detonation models in underwater explosions. *Electronic Modeling* (2003) **25**: 113-124.

[14] Liu, M.B., Liu, G.R. and Lam, K.Y. A one dimensional meshfree particle formulation for simulation shock waves. *Shock Waves* (2003) **13**:201-211.

[15] Liu, M.B., Liu, G.R. and Zong, Z. et al. Smoothed particle hydrodynamics for numerical simulation of underwater explosions. *Computational Mechanics* (2002) **30**:106-118.

[16] Feng, D.L., Liu, M.B. and Li, H.Q. et al. Smoothed particle hydrodynamics modeling of linear shaped charge with jet formation and penetration effects. *Computers & Fluids* (2013) **86**: 77-85.

[17] Yang, G., Han, X., Hu, D.A. Computer simulation of two-dimensional linear-shaped charge jet using smoothed particle hydrodynamics. *Engineering Computations: International Journal for Computer-Aided Engineering and Software* (2011) **28**: 58-75.

[18] Qiang, H.F., Wang, K.P. and Gao, W.R. Numerical Simulation of Shaped Charge Jet Using Multi-Phase SPH Method. *Tianjin Univ.* (2008) **14**: 495-499.

[19] Zhang, A.M., Yang, W.S. and Yao, X.L. Numerical simulation of underwater contact explosion. *Applied Ocean Research* (2012) **34**: 10-20.

[20] Zhang, A.M., Yang, W.S. and Huang, C. et al., Numerical simulation of column charge underwater explosion based on SPH and BEM combination. *Computers & Fluids* (2013) **71**: 169-178.

[21] Liu, G.R. and Liu, M.B. Smoothed Particle Hydrodynamics - A Meshfree Particle Method. *Singapore: World Scientific Publishing Co. Pte. Ltd* (2003).

[22] Zhang, Z.F., Ming, F.R. and Zhang, A.M. Damage Characteristics of Coated Cylindrical Shells Subjected to Underwater Contact Explosion. *Shock and Vibration* (2014) **2014.**

[23] Dobratz, B.M. LLNL Explosive Handbook: properties of chemical explosives and explosives and explosive simulants. *Report UCRL 52997*, Lawrence Livermore National Laboratory, Livermore, Calif, USA. (1981).

[24] Steinberg, D.J. Spherical explosions and the equation of state of water. *Lawrence Livermore National Laboratory*. Livermore, CA, (1987)

[25] Libersky, L.D., Petschek, A.G. and Carney, T.C. et al. High strain lagrangian hydrodynamics a three dimensional SPH code for dynamic material response. *Journal of Computational Physics* (1993) **109**: 67-75.

[26] Johnson, G.R. and Cook, W.H. A constitutive model and data for metals subjected to large strains, high strain rates and high temperatures. *In Proc. 7th International Symposium on Ballistics*, USA, (1983).

[27] Meyer, M.A. Dynamic behavior of materials. *JOHN WILEY & SONS INC*, USA. (1994).

[28] Clegg, R.A., Hayhurst, C.J. Development of a Smooth Particle Hydrodynamics Option for Continuum Hydrocodes, Final Report, User Instructions. *DRA Contract No. WSF/798, Century Dynamics Report No. R066:01*, (1996).

[29] Clegg, R.A., Sheridan, A.J. Hayhurst, C.J. et al. The Application of SPH Techniques in AUTODYN-2D to Kinetic Energy Penetrator Impacts on Multi-Layered Soil and Concrete Targets. *8th International Symposium on Interaction and Effects of Munitions with Structures*, USA, (1997).

[30] Hayhurst, C.J., Clegg, R.A. Cylindrically Symmetric SPH Simulations of Hypervelocity Impacts on Thin Plates", *Int. J. Impact Engng* (1997) **20**: 337-348.